Macroscopic X-ray powder diffraction scanning : possibilities for quantitative and depth-selective parchment analysis

Macroscopic X-ray powder diffraction scanning: possibilities for quantitative and depth-selective parchment analysis

Frederik Vanmeert, Wout De Nolf, Joris Dik, and Koen Janssens

Anal. Chem., **Just Accepted Manuscript** • DOI: 10.1021/acs.analchem.8b00241 • Publication Date (Web): 06 Apr 2018

Macroscopic X-ray powder diffraction scanning: possibilities for quantitative and depth-selective parchment analysis

Frederik Vanmeert,[‡*] Wout De Nolf,[‡†] Joris Dik[§] and Koen Janssens[‡]

[‡] AXES Research Group, Department of Chemistry, University of Antwerp, Groenenborgerlaan 171, B-2020 Antwerp, Belgium

[§] Department of Materials Science, Delft University of Technology, Mekelweg 2, 2628 CD Delft, the Netherlands

ABSTRACT: At or below the surface of painted works of art, valuable information is present that provides insights into an object's past, such as the artist's technique and the creative process that was followed or its conservation history, but also on its current state of preservation. Various noninvasive techniques have been developed over the past two decades that can probe this information either locally (via point analysis) or on a macroscopic scale (e.g. full-field imaging and raster scanning). Recently macroscopic X-ray powder diffraction (MA-XRPD) mapping using laboratory X-ray sources was developed. This method can visualize highly-specific chemical distributions at the macroscale (dm^2). In this work we demonstrate the synergy between the quantitative aspects of powder diffraction and the noninvasive scanning capability of MA-XRPD highlighting the potential of the method to reveal new types of information. Quantitative data derived from a $15^{th}/16^{th}$ century illuminated sheet of parchment revealed three lead white pigments with different hydrocerussite-cerussite compositions in specific pictorial elements, while quantification analysis of impurities in the blue azurite pigment revealed two distinct azurite types: one rich in barite and one in quartz. Furthermore, on the same artefact, the depth-selective possibilities of the method that stem from an exploitation of the shift of the measured diffraction peaks with respect to reference data are highlighted. The influence of different experimental parameters on the depth-selective analysis results is briefly discussed. Promising stratigraphic information could be obtained, even though the analysis is hampered by not completely understood variations in the unit cell dimensions of the crystalline pigment phases.

A wealth of information is present at or below the surface of painted works of art. Accessing this stratigraphic information may yield valuable insights into an artist's technique and/or thought process, the conservation history and state of preservation of the work and can uncover underlying compositions. In the last two decades several new photon-based analytical techniques for (sub)surface imaging have been developed that probe the inner structure of painted works and complement traditional X-ray radiography, infrared reflectography and the analysis of cross-sectioned samples.[1,2] Most of these innovative techniques provide curators, conservators and scientists with projected images that do not contain any (valuable) depth information. Indeed, only a limited number allow for some form of depth discrimination: computed tomography and laminography can be used to visualize three-dimensional density variations, optical coherence tomography and terahertz imaging can map interfaces inside the layer stratigraphy, such as between varnishes, glazes and various paint layers, and the local elemental composition at various depths along the layer structure can be probed with confocal X-ray fluorescence. Recently microscale spatially offset Raman spectroscopy (micro-SORS), a powerful technique that can penetrate larger depths compared to confocal RS, has been shown to retrieve molecular information from individual subsurface paint layers in samples from polychrome sculptures.[3] However because of strict experimental requirements, the technique is usually not applied *in situ* and has only recently been applied for imaging of a hidden mock-up.[4,5]

X-ray powder diffraction (XRPD) is a well-established technique for the identification of crystalline materials in complex mixtures and is routinely used for the analysis of cultural heritage objects.[6] Analyses with conventional benchtop diffractometers typically require a finely ground homogenized powder of (a limited amount of) material taken from the artwork. Also Gandolfi cameras can be used to obtain 'powder-like' diffraction data from samples containing only a few single crystals.[7] More recent advances in capillary optics allow for the nondestructive analysis of minute paint samples using microscopic beams inside the laboratory and can be used for the identification of crystalline compounds within individual layers.[8-11] At synchrotron radiation facilities compound-specific distribution images can be obtained with submicrometric spatial resolution revealing the entire, and often complex, sequence of paint and degradation layers.[12]

Next to phase identification, XRPD is a powerful tool for the quantitative analysis of crystalline compounds. For precious (and often unique) samples, the analysis is frequently performed using the Rietveld method which does not require the addition of internal standards. Furthermore Rietveld refinement is applicable to mixtures of compounds that exhibit strong diffraction line overlap, as is the case for the various lead carbonates present in the pigment lead white.[13] From the obtained phase fractions, information about the pigment production process can be deduced. It was recently demonstrated that the composition of the lead white pigment, a mixture of the basic and neutral lead carbonates (respectively hydrocerus-

site and cerussite) changes as a function of the post-synthesis treatment employed.[14-16] For other materials information regarding their provenance and kinetics of degradation mechanisms can be gained by analyzing the mineral abundance.[6] Although the sensitivity and accuracy of laboratory microscopic (μ-)XRPD instruments is limited compared to that of conventional benchtop diffractometers, a good estimation of the phase quantities can be obtained in a nondestructive manner.[11]

The need for noninvasive analysis, i.e. without taking samples, in the cultural heritage field has driven the development of portable instrumentation. These portable instruments allow various complementary techniques, such as X-ray fluorescence (XRF), Fourier transform infrared (FTIR), UV-Vis and RAMAN spectroscopy, and XRPD, to be employed without the need to sample or move the object.[17] For portable (p-)XRPD the analysis is restricted to a limited number of points as exposure times of several tens of minutes to one hour are required to obtain useful diffraction data from a single spot;[18] quantitative studies employing p-XRPD instruments have not yet been reported. Innovative noninvasive imaging methods at the macroscale have been developed for *in situ* analyses of flat painted works of art, such as macroscopic (MA-)XRF, MA-reflectance FTIR and hyperspectral full-field imaging.[19-21] To complement these techniques a combined MA-XRF/XRPD scanning instrument has recently been described that is suited for highly-specific pigment mapping of flat painted objects (ref. part 1). The instrument typically requires dwell times between 0.2 – 10 seconds (depending on the work of art) to collect X-ray powder diffraction and fluorescence data simultaneously, allowing for macroscopic areas (dm^2) to be imaged.

Analysis of X-ray powder diffraction data largely relies on the accurate determination of the positions of diffraction peaks which are matched to information from reference databases. This is possible only if the sample is placed at a fixed calibrated distance from the diffraction detector. Noninvasive analysis of layered structures allows at most one layer to be placed at the calibrated distance, causing a shift in the measured diffraction peak positions with respect to the reference values for compounds present in other layers. However, this shift can be usefully exploited to calculate the displacement of each compound to the calibrated distance[22,23] and has recently been exploited by Chiari et al using the DUETTO pXRPD system to determine the thickness of a calcite layer in a single point on a Roman-Egyptian funerary portrait.[24]

In this work the capability of MA-XRPD for quantitative analysis and for delivering depth-sensitive information that can be linked to the macroscopic distribution images is illustrated on a sheet of parchment from an illuminated 15th/16th century Book of Tides. The various compound-specific distribution images have been discussed in a previous part of this work (ref. part 1).

MATERIAL AND METHODS

MA-XRF/XRPD system

The combined MA-XRF/XRPD instrument employs a low power Cu-anode X-ray micro source (30 W, IμS-Cu, Incoatec GmbH, DE) that delivers a monochromatic (Cu-K_α) and focused X-ray beam (focal spot diameter: 313 (5) μm; output focal distance: 39.8 (1) cm; divergence: 2.6 (4) mrad). A PILATUS 200K detector placed perpendicular to the source at the output focal distance collects diffraction patterns in transmission mode, while fluorescence radiation is simultaneously acquired with a Vortex-EX silicon drift detector (SII, Northridge, CA, US). The parchment was positioned in front of the area detector at a distance of 2.9 cm (see Figure 1A). XYZ motorized stages (max. travel ranges: 10 cm × 25 cm × 10 cm, Newport Corporation, Irvine, CA, USA) allow for the movement of the artwork during the imaging experiment while the instrument remains stationary. A LaB_6 standard for powder diffraction (SRM 660, NIST) is used for the calibration of the instrument. The analytical characteristics of the combined MA-XRF/XRPD system have recently been reported elsewhere (configuration 9, ref. part 1).

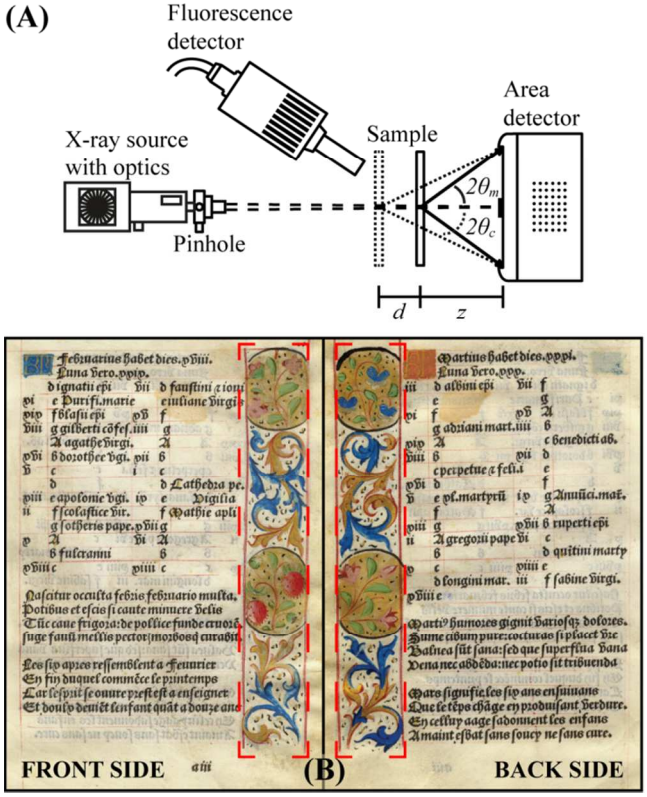

Figure 1 (A) Schematic of the combined MA-XRF/XRPD instrument. The dotted lines represent the diffraction signals coming from a sample that shows a displacement (*d*) compared to the calibrated sample-detector distance (*z*). (B) Photographs of the front and back side of the illuminated sheet of parchment with markings of the analyzed area (red dashed lines).

Data processing

Diffraction data was integrated and analyzed using the XRDUA software package which is designed to handle the large amount of data generated during scanning experiments.[25] The imaging software allows for the real-time analysis of the diffraction data and the visualization of spatial distribution images through regions of interest (so-called explorative processing) without prior knowledge of the materials present in the sample, while more elaborate modelling of the data can be performed after data collection. A detailed overview of the functionality of the XRDUA imaging software is given elsewhere.[23]

After the automated azimuthal integration process whole pattern fitting was performed on the one-dimensional data

taking into account both the Cu-$K_{\alpha1}$ and -$K_{\alpha2}$ contributions to the diffraction patterns. A Rietveld model containing all identified crystalline compounds was constructed using crystal structures obtained from the American Mineralogist Crystal Structure Database[26] or from literature. The relative peak positions and intensities of each individual compound remained fixed during fitting, while the width of the diffraction signals was modelled using only the theta-independent part of the Cagliotti peak width function. In this way refined values for the displacement, scaling and width parameters for each compound in each data point were obtained. Several constraints were set on the displacement and width parameters to avoid solutions without physical meaning. The background contribution was modelled using a strip function. Visualizing the scaling parameter as a grey scale value in each point yields compound-specific distribution images.

One-dimensional diffraction data shown throughout this work is expressed as a function of the scattering vector ($Q = 2\pi/d = 4\pi \sin(\theta)/\lambda$).

Illuminated manuscript

The manuscript (private collection) is an excerpt from an illuminated 15th/16th century Book of Tides and features numerous decorations, see Figure 1B. In black ink, a Latin text accompanied by a French translation covers most of the parchment. In the margin, colorful vegetal motifs such as strawberries and flowers were applied on both *recto* and *verso* sides. The entire marginal decoration of the illuminated sheet of parchment was imaged using the MA-XRF/XRPD instrument over a period of 8.4 hours (total map size: 137.6 × 22.8 mm^2; pixel size: 0.4 × 0.4 mm^2; 344 × 57 pixels; dwell time per point: 0.2 s). Up to twelve different compound-specific distribution images were revealed in this manner in a first part of this work (ref. part 1): azurite ($2CuCO_3.Cu(OH)_2$), malachite ($CuCO_3.Cu(OH)_2$), quartz (SiO_2), barite ($BaSO_4$), gold (Au^0), cinnabar (HgS), calcite ($CaCO_3$), gypsum ($CaSO_4.2H_2O$), lead tin yellow type I (Pb_2SnO_4), massicot (*o*-PbO), hydrocerussite ($2PbCO_3.Pb(OH)_2$) and cerussite ($PbCO_3$), see Table S-1 for the corresponding PDF codes.

RESULTS AND DISCUSSION

Quantitative information

Three types of Lead white

Photographs of the decorated cartouches depicted at the top of the manuscript on the *recto* and *verso* side are given in Figure 2A-B. The pink flowers, the white highlights and several blue-greyish areas (marked by red and blue dashed contours) appear together in the cerussite MA-XRPD distribution (Figure 2D) indicating that the neutral lead carbonate was used in these pictorial elements. Features from both the *recto* and *verso* side are simultaneously present in the distribution image as MA-XRPD provides superimposed mapping information. The basic lead carbonate, hydrocerussite (HC), is co-localized with cerussite (C), except in the green leaves (marked by green dashed contours) for which lead white paint was used that only contains HC (Figure 2C). Qualitatively it can be seen that (at least) two different lead white mixtures were used based on these compound-specific spatial distribution images for HC and C.

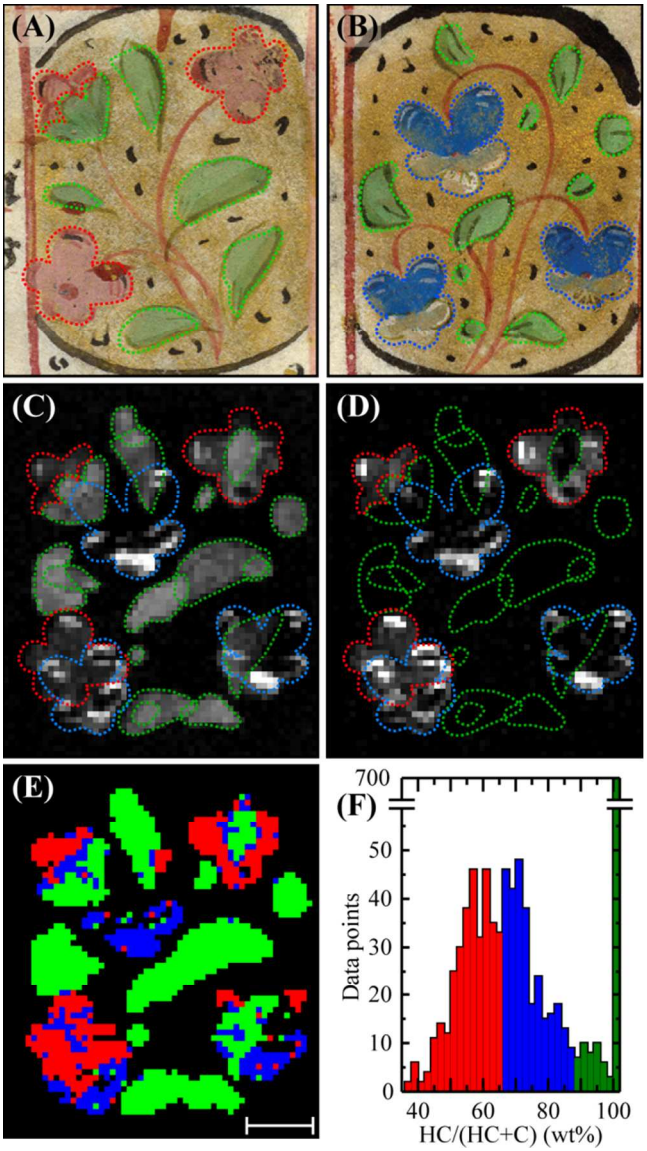

Figure 2 Photographs of the top cartouche depicted (A) on the *recto* and (B) *verso* side (mirrored) of the parchment. Selected regions of the compound-specific distribution images obtained for (C) hydrocerussite and (D) cerussite. Lighter grey values indicate a higher scaling parameter. The green, blue and red dashed lines are added to highlight the different pictorial features visible in (A) and (B). (E) False color image of the lead white distribution using the color scheme shown in the histogram (scale bar = 5 mm). (F) Histogram of the HC/(HC+C) mass ratio containing 1383 data points. A threshold based on the hydrocerussite scaling parameter was employed to exclude data points from the histogram in which lead white was not detected.

With whole pattern fitting, the relative weight fractions of both carbonates in each point of the image can be determined (see examples given in Figure S-1). For each individual point in the distribution images, the mass ratio (*MR*) for HC in the lead white pigment was calculated using the relative weight fractions (w) of HC and C ($MR_i = w_i/\sum_i w_i$) and the results are shown in the histogram in Figure 2F. The histogram was constructed from 1383 individual XRPD patterns. In this histogram one broad distribution around MR_{HC} = 65 wt% and one narrow distribution at MR_{HC} = 100 wt% can be found indicat-

ing the presence of two lead white pigments with different HC-C content.

However, when linking the quantitative information to the macroscopic spatial distribution it becomes clear that in fact (at least) three different types of lead white were used, even though only two distributions are apparent in the histogram. Indeed, the broad mass ratio distribution contains contributions from two different lead white mixtures (shown in red and blue). The false color image shows the distribution of the three different lead white pigments throughout the gilded cartouches (Figure 2E). Lead white consisting of only HC was used in the green leaves, while the pink flowers and the blue-greyish regions of the blue flowers have been painted with two different HC-C mixtures. The compositions of the three lead whites are estimated from the histogram to contain MR_{HC} = 56 (±6) wt% (red), 74 (±6) wt% (blue) and 100 (±2) wt% (green). These compositions are in good agreement with previous HC abundances determined in 16th century lead white mixtures.[13] Both cerussite containing pigments correspond to HC abundances consistently found in lead white synthesized following the stack process, while HC-pure lead white is thought to be formed using a very short synthesis time or by heating of the pigment in water.[14,16] Since the *recto* and *verso* sides are measured simultaneously averaged compositions are obtained for regions that contain lead white on the front and back side of the parchment (e.g. overlap between the green leaves on the *recto* and the pink flowers on the *verso*, or vice versa) or for those regions in which the different lead white types are adjacent to each other (e.g. the pink flower with the green sepal in the top left corner). These regions also appear as blue in the false color image.

It remains unclear if the broad histogram distributions for the red and blue lead white mixtures are due to the uncertainty on the measured or modelled diffraction intensities, or if paint mixtures with a broad range in HC-C composition have been used. The latter would strongly depend on the lead white manufacturing process which often yielded a product of widely varying purity.[27,28] The quality of lead white also depends on the amount of extender, such as calcite, that was added to the pigment for economic reasons.[14,28] The calcite content within the lead white paint could not be quantified as calcite is also abundantly present throughout the entire parchment.

For the cartouches in the bottom part of the parchment two different lead white mixtures could be distinguished with estimated compositions of MR_{HC} = 70 (±9) and 100 (±2) wt%, see Figure S-2.

Two types of Azurite

The blue paint used for the decorative scrollwork and the blue flowers consists of azurite, a copper carbonate frequently used in European painting. Barite and quartz are less common impurities related to azurite owing to its mineralogical origin[29,30] and are found to be co-localized with azurite on the parchment (see ref. part 1 for more details). It has been suggested that identification of these unusual impurities could play an important role in provenance studies of azurite ore and a recent study has shown that up to four different azurite types can be present on the same manuscript cutting.[31]

Figure 3 shows the mass ratios for azurite, barite and quartz in the blue paint obtained from 4380 individual XRPD patterns. Whole pattern fits of selected data points are shown in Figure S-3. Two types of azurite were found to be used for the blue decorations. The majority of the blue pigment has a (relatively) high barite content ($MR_{azurite}$ = 93 (±1) %, MR_{barite} = 4 (±1) % and MR_{quartz} = 3 (±2) %, shown in green) and has been used for the blue flowers and most of the scrollwork. A second type of azurite with no detectable barite and a higher quartz content was only found in some regions of the bottom blue scrollwork on the back side of the parchment ($MR_{azurite}$ = 94 (±2) %, MR_{barite} = 0.7 (±4) % and MR_{quartz} = 5 (±2) %, shown in red). The data points with mass ratios in the blue region in Figure 3A are artefacts linked to two areas in the upper blue flowers. These represent the higher SiO_2 contents that were detected because of overlap of the quartz reflections (101) and ($10\bar{1}$) with those of lead tin yellow (121) used in the green leaves on the front side (see ref. part 1 for details) and are not indicative of a third type of azurite. The different types of azurite could originate from different ore mines, differences within a single geological site or to different grades of/other procedures for purification.[31] It is not clear why, in this manuscript, the artist chose to use two different types of azurite for the same purpose. The presences of two varieties of azurite could simply indicate the use of different batches of pigment or point to azurite added during a later restoration.

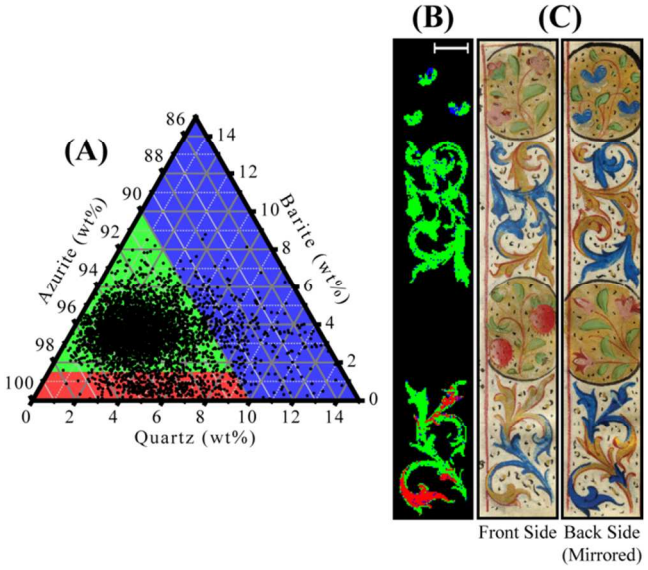

Figure 3 (A) Ternary plot of the azurite, barite and quartz mass ratios for the blue color used throughout the parchment. Each of the 4380 data points represents a single pixel in the mapping experiment. A threshold based on the azurite scaling parameter was employed to remove data points in which azurite was not detected. (B) False color image of the azurite distribution using the color scheme shown in the ternary plot (scale bar = 10 mm). (C) Photographs of the marginal decorations on the *recto* and *verso* sides of the parchment.

Depth-selective information

With conventional X-ray diffractometers a (paint) sample is ground and mixed to a fine homogenous powder before analysis. The powder is placed at the calibrated distance of the instrument so that the measured diffraction peak positions for all compounds correspond to the different interplanar distances present in the crystal structures. These measured peak positions can then be matched to those reported in crystal structure

reference databases in order to identify the different compounds present in the sample.

For a multilayered paint system, at most one layer of the sample can be placed at the calibrated distance (typically the surface layer) at a given time. Crystalline material present within layers that are positioned in front or behind this optimal measurement position will exhibit a shift in their measured diffraction peak positions compared with those reported in literature. In Figure 4A it can be seen that for a paint sample consisting of a set of perfectly flat layers, the strata positioned closer to the detector than the calibrated distance (z) will show a peak shift, resulting in smaller Q values (Q_S and Q_P) compared to the reported peak positions (Q_{Sref} and Q_{Pref}). For signals at higher 2θ angles (or Q values), up to 45° 2θ, the same displacement will result in a larger peak shift (see Figures S-4A and C). For overlapping layers of the same pigment (Q_{P2}) either an intermediate shift and a broader diffraction peak or two separate peaks will be obtained depending on the distance between the two layers. The position of the substrate signal will stay unchanged between different points (Q_S). If the different crystalline compounds are known, the shift between measured and reference peak position can be exploited to obtain stratigraphic information.[24] In the whole pattern fitting procedure this information is contained within the displacement parameter (i.e. the distance of the center of mass of each compound to the detector).[22,23]

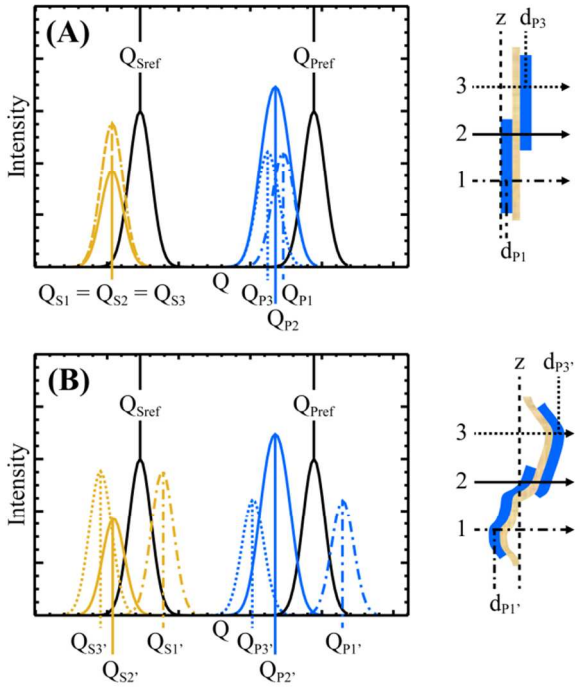

Figure 4 Shift of the diffraction peaks caused by displacement of the blue pigment layer (P, blue) and the substrate (S, beige) to the calibrated distance to the detector (z) at different points (1-3) for (A) a perfect flat sample and (B) a sample showing strong curvature. The average distance of the blue layers to the detector in position 1 and 3 are given by respectively d_{P1} and d_{P3} for the flat sample and $d_{P1'}$ and $d_{P3'}$ for the sample with curvature. The arrows indicate the direction of the primary X-ray beam. The black signals correspond to the diffraction peak positions from reference databases.

For real objects, sample curvature, e.g. due to the bent surface of painted wooden panels or due to the presence of folds and wrinkles in a manuscript folio, will also contribute to the peak shift. In Figure 4B the shift of the diffraction signals not only depends on the stratigraphy of the layer structure but also on the sample displacement (e.g. d_{P1} vs $d_{P1'}$). In this case the shift in peak positions for $Q_{P1'}$ and $Q_{P3'}$ becomes larger or smaller depending on the curvature of the sample. A peak shift for the substrate layer is also observed, because the displacement with the calibrated distance is no longer constant between the different points ($Q_{S'}$). For single point measurements, sample curvature is not an issue as the sample can be moved to the same calibrated distance between exposures, but in a mapping experiment it is not (always) possible to continuously reposition the sample (or the instrument) at each measurement point. Therefore in order to extract information about the layer stratigraphy with MA-XRPD the sample curvature needs to be taken into account.

Indeed, when looking at the displacement parameter for calcite the curvature of the illuminated parchment is clearly visible (see Figure 5 left). Since chalk is present inside the parchment substrate as it was used during its preparation, it is an ideal marker to visualize its curvature. In each pixel of the imaging experiment the calcite displacement parameter (d) can be used to correct the recorded peak positions ($2\theta_m$) of all compounds. The corrected peak positions ($2\theta_c$) for an area detector in transmission mode placed perpendicular to the primary X-ray beam at a calibrated sample-detector distance (z) are given by Eq. 1

$$2\theta_c = \mathrm{atan}(z \cdot \tan(2\theta_m)/(z + d)) \qquad \text{Eq. 1}$$

with d < 0 for compounds positioned closer to the detector.

After applying the curvature correction to all collected diffractograms and repeating the whole pattern fitting procedure on the corrected data set, it can be seen that a uniform distribution for the displacement parameter of calcite is obtained (Figure 5 right). All curvature has therefore been removed, corresponding to a virtual flattening of the manuscript in the scanned area.

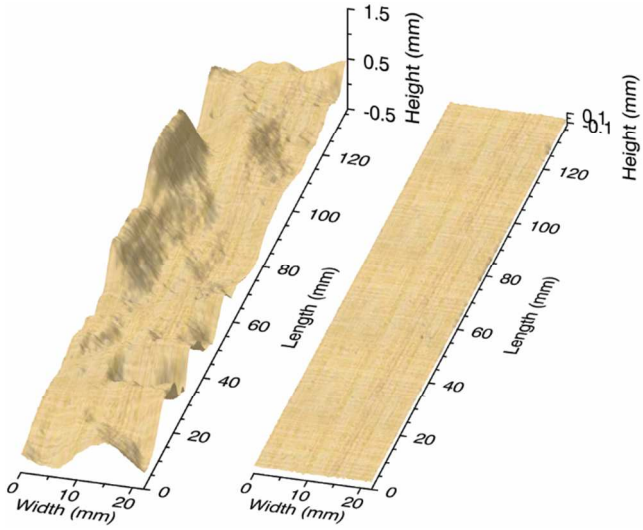

Figure 5 3D visualization of the displacement parameter of calcite present in the parchment before (left) and after (right) curvature correction. The height-scale has been magnified by a factor 10 to improve readability.

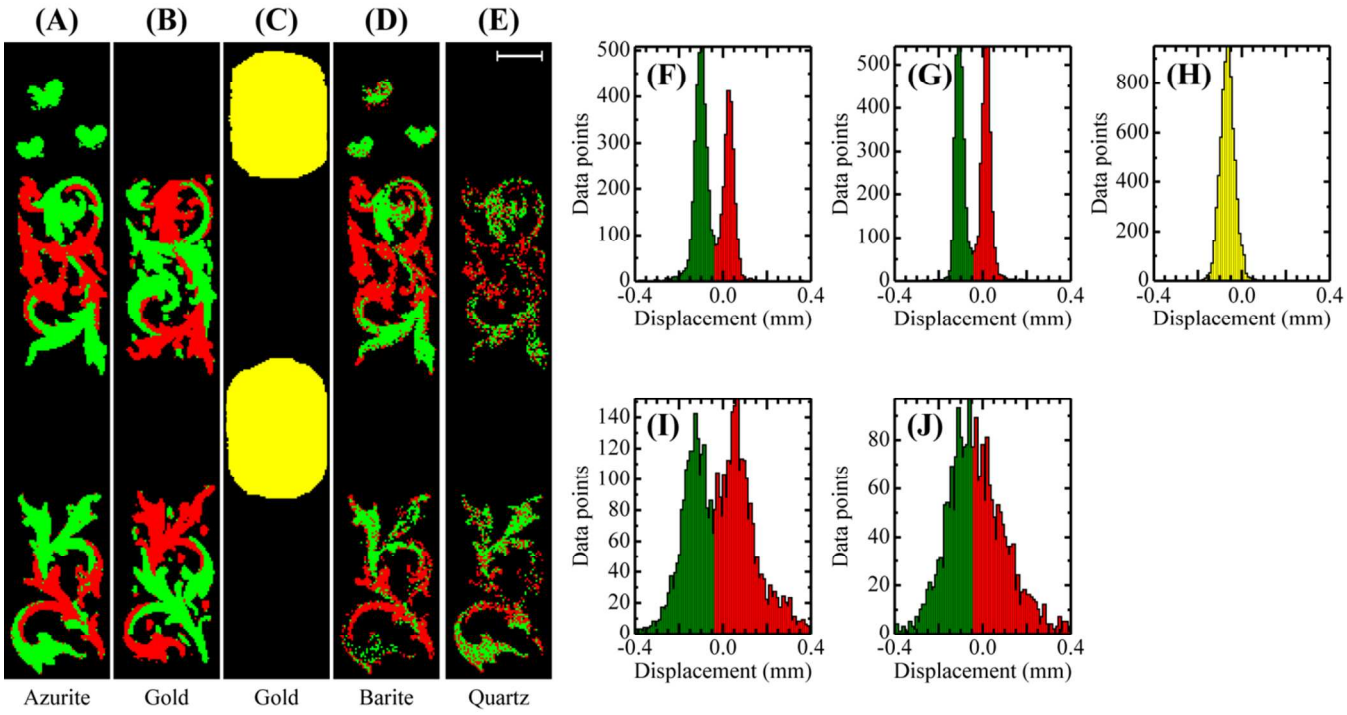

Figure 6 False color images of the (A) azurite, (B) gold used in the scrollwork, (C) gold used in the cartouches, (D) barite and (E) quartz distributions (scale bar = 10 mm). The histograms of the displacement parameters after curvature correction for (F) azurite, (G) gold in the scrollwork and (H) gold in the cartouches, (I) barite and (J) quartz show the color schemes that were used. A threshold based on the scaling parameter for each compound was employed to remove data points in which the compounds were not detected.

Figure 6 shows the distributions of the displacement parameters for azurite, gold, barite and quartz after curvature correction. An intensity threshold was employed to remove data points from the imaging experiment in which the respective compounds were not present. The distinction between azurite and gold present in the scrollwork on either the front or back side can easily be made based on their displacement histograms (Figure 6F and G). The false color images, with red indicating pigments on the *recto* side of the manuscript (further from the detector) and green on the *verso* side, show the artistic interplay of the two pigments: areas of the scrollwork that have been painted with azurite on the front side are gilded on the back side and vice versa (Figure 6A and B). Confocal XRF analyses previously conducted on the illuminated parchment have shown that the gold layer is very thin (< 1 µm)[32] so that the average thickness of the parchment can be estimated from the gold histograms and is about 120 µm. Indeed, only the parchment separates the gilding on the *recto* and *verso* sides. Unsurprisingly, barite features a similar depth distribution than azurite, showing it to be present on the front and back side in the same regions (Figure 6D). However, the low intensity of the barite XRPD peaks results in a large uncertainty on the modelled position of the diffraction signals, resulting in two broad distributions in the displacement histogram (Figure 6I). Even though for the quartz impurity the large spread in displacement values yields only one apparent layer in the histogram, a noisy image of its spatial distribution in the two different blue layers can still be extracted (Figure 6E and J).

While in the cartouches the gilding has been applied on both sides of the parchment, a unimodal distribution is visible in the corresponding displacement histogram (Figure 6C and H). The two gold layers are separated only by the parchment, with a thickness of 120 µm. Rather than appearing as two separate contributions, the diffraction signals for gold originating from the front and back side appear as single combined peaks in the diffraction data. Indeed, when layers of the same pigment are applied on top of each other, the angular resolution of the MA-XRF/XRPD instrument is insufficient to separate the diffraction signals coming from the individual layers unless a thicker intermediate layer (or sequence of layers) is present. The minimal thickness of the intermediate layer to obtain a clear separation of the two pigment layers is around 700 µm (see Figure S-4D). Our experience has shown that not only the angular resolution, but also a smaller sample-detector distance or a higher primary energy (Figures S-4A and B) can strongly improve the depth-selectivity.

Although a separation can be made between the front and back side of the parchment, it is noteworthy that the absolute displacements for the different compounds are sometimes misleading. Indeed, the average displacement of lead tin yellow present on the front side of the parchment would place it together with azurite on the back side, respectively $d_{leadtinyellow,recto}$ = -0.10 mm and $d_{azurite,verso}$ = -0.10 mm (Figure S-5H). A similar displacement was found for malachite (Figure S-5I). Unfortunately not only the displacement of the pigments influences the position of the measured diffraction signals, either because of stratigraphy or curvature, but also a difference between their actual unit cell dimensions compared to those reported in reference databases results in a shift in peak position. These variations in unit cell can be caused by isomorphic

crystal structures. For example, the substitution of calcium with magnesium in the calcite crystal lattice may cause a reduction in the unit cell dimensions and consequently shifts the positions of the diffraction peaks of calcite to smaller values. Similarly small amounts of zinc can be incorporated in the crystal structure of the mineral malachite which alters the unit cell dimensions of the malachite lattice.[33] The origin of the shift in the synthetic pigment, lead tin yellow type I, remains unclear. The ability to determine absolute displacements for different compounds in a layered sample will therefore depend on how well the actual unit cell dimensions of the materials inside the object are known and will prove quite a challenge for the noninvasive analysis of real objects. Nonetheless the relative position between two or more layers containing the same pigment can be extracted, even when the unit cell dimensions are not accurately known.

For the pigments used for the vegetal and floral decorations throughout the cartouches a similar separation between the *recto* and *verso* sides could be made. However broad and overlapping histogram distributions, originating from low intensity diffraction signals and overlapping layers of the same pigment, are more often present (Figure S-5).

CONCLUSIONS

Combined MA-XRF/XRPD is a powerful noninvasive technique that not only allows for the identification and visualization of highly-specific pigment distributions, but it can also extract quantitative information about the composition of pigments used throughout the work of art. In this work it has been shown that visualizing these phase fractions at the macroscale can help to differentiate even subtle differences in composition. These different compositions are often linked to various pigment qualities and their identification is a first step to understanding if certain pigment types were generally favored for the same purpose by a specific artist or period in time. MA-XRPD could prove particularly useful for clarifying the different compositions of lead white, a pigment that has been extensively used until the 19th century. However care should be taken in the interpretation of these results since averaged compositions will be obtained when multiple lead white layers are stacked on top of each other (e.g. lead white present in the ground and pictorial layers) because of the transmission geometry of the instrument. Quantification of the barite and quartz impurities within the azurite pigment revealed that two different azurite types (barite-rich and azurite-rich) were used on the illuminated parchment. Linking this information to the spatial distribution images showed distinct areas in which these two types were used.

In a second part, the displacement parameter was used to extract limited information about the layer stratigraphy. It was possible to separate the same pigment applied on the front side of the parchment from the back side based on the collected diffraction data. However it was not possible to separate overlapping layers of the same pigment with the current instrument because of the thin separation layer (around 120 µm). Increasing the path length between the overlapping layers by positioning the sample under a smaller incident angle (< 90 degrees, reflection geometry) will increase the diffraction peak shift and reduce this limitation. Two obstacles hamper the stratigraphic analysis: sample curvature and variations in unit cell dimensions. In this work, the former was corrected using calcite as a marker for the parchment roughness as it was present throughout the entire imaged area. The selected marker should ideally not be present within the paint layers themselves. Alternatively position sensitive devices can be used to measure and correct for sample displacement (e.g. laser sensor) before or after data collection. Furthermore, curvature correction simplifies data interpretation, as the shift in the position of the measured diffraction signals between individual points in the mapping experiment is greatly reduced. During whole pattern fitting this allows for more strict constraints on the displacement parameter so that erroneous contributions to compound-specific distribution images due to peak overlap can be minimized. Variations between the unit cell dimensions of the reference crystal structures and those of the actual materials present inside the object form the second obstacle. A systematic study of possible crystal structure variations for each pigment or a complementary analysis of cross-sections, when available, will result in more accurate depth information.

Next to identification of pigments, quantification of pigment compositions and delivering stratigraphic information of paint layers, also information about the texture and orientation, microstructure (crystallite and grain size) and/or isomorphs of pigments can provide valuable information. The ability of MA-XRPD to make some of this information available in a noninvasive manner and on a macroscopic scale holds a promising future for cultural heritage research.

ASSOCIATED CONTENT

Supporting Information

Additional information as noted in the text. The Supporting Information is available free of charge on the ACS Publications website.

AUTHOR INFORMATION

Corresponding Author

* Email: frederik.vanmeert@uantwerpen.be

Present Addresses

† Experimental Division, European Synchrotron Radiation Facility, 71 Ave Martyrs, F-38000 Grenoble, France

Notes

The authors declare no competing financial interest.

ACKNOWLEDGMENT

The authors thank Incoatec GmbH for giving us the opportunity to test the IµS-Cu X-ray source. We acknowledge financial support from BELSPO (Brussels) S2-ART, the NWO (The Hague) Science4Arts 'ReVisRembrandt' project and GOA Project Solarpaint (University of Antwerp Research Council).

REFERENCES

(1) Janssens, K.; Dik, J.; Cotte, M.; Susini, J. *Acc. Chem. Res.* **2010**, *43*, 814-825.

(2) Alfeld, M.; Broekaert, J. A. C. *Spectrochim. Acta, Part B* **2013**, *88*, 211-230.

(3) Conti, C.; Colombo, C.; Realini, M.; Matousek, P. *J. Raman Spectrosc.* **2015**, *46*, 476-482.

(4) Casadio, F.; Daher, C.; Bellot-Gurlet, L. *Top. Curr. Chem.* **2016**, *374*.

(5) Botteon, A.; Conti, C.; Realini, M.; Colombo, C.; Matousek, P. *Anal. Chem.* **2017**, *89*, 792-798.

(6) Artioli, G. *Rendiconti Lincei-Scienze Fisiche E Naturali* **2013**, *24*, S55-S62.
(7) Janssens, K. In *Non-destructive microanalysis of cultural heritage materials*, Janssens, K.; Van Grieken, R., Eds.; Elsevier Science, 2004, p 828.
(8) Aze, S.; Vallet, J. M.; Baronnet, A.; Grauby, O. *Eur. J. Mineral.* **2006**, *18*, 835-843.
(9) Benedetti, D.; Alessandri, I.; Bergese, P.; Bontempi, E.; Colombi, P.; Garipoli, D.; Pedrazzani, R.; Zanola, P.; Depero, L. E. *Microchim. Acta* **2006**, *155*, 101-104.
(10) Duran, A.; Perez-Rodriguez, J. L.; Jimenez de Haro, M. C. *Anal. Bioanal. Chem.* **2009**, *394*, 1671-1677.
(11) Svarcova, S.; Koci, E.; Bezdicka, P.; Hradil, D.; Hradilova, J. *Anal. Bioanal. Chem.* **2010**, *398*, 1061-1076.
(12) Janssens, K.; Van der Snickt, G.; Vanmeert, F.; Legrand, S.; Nuyts, G.; Alfeld, M.; Monico, L.; Anaf, W.; De Nolf, W.; Vermeulen, M.; Verbeeck, J.; De Wael, K. *Top. Curr. Chem.* **2016**, *374*.
(13) Welcomme, E.; Walter, P.; Bleuet, P.; Hodeau, J. L.; Dooryhee, E.; Martinetto, P.; Menu, M. *Appl. Phys. A: Mater. Sci. Process.* **2007**, *89*, 825-832.
(14) Gonzalez, V.; Calligaro, T.; Wallez, G.; Eveno, M.; Toussaint, K.; Menu, M. *Microchem. J.* **2016**, *125*, 43-49.
(15) Stols-Witlox, M.; Megens, L.; Carlyle, L. In *The artist's process: technology and interpretation*, Eyb-Green, S.; Townsend, J. H.; Clarke, M.; Nadolny, J.; Kroustallis, S., Eds.; Archetype Publications: London, 2012, pp 112-129.
(16) Gonzalez, V.; Wallez, G.; Calligaro, T.; Cotte, M.; De Nolf, W.; Eveno, M.; Ravaud, E.; Menu, M. *Anal. Chem.* **2017**, *89*, 13203-13211.
(17) Brunetti, B.; Miliani, C.; Rosi, F.; Doherty, B.; Monico, L.; Romani, A.; Sgamellotti, A. *Top. Curr. Chem.* **2016**, *374*.
(18) Nakai, I.; Abe, Y. *Appl. Phys. A: Mater. Sci. Process.* **2012**, *106*, 279-293.
(19) Alfeld, M.; Janssens, K.; Dik, J.; de Nolf, W.; van der Snickt, G. *J. Anal. At. Spectrom.* **2011**, *26*, 899-909.
(20) Legrand, S.; Alfeld, M.; Vanmeert, F.; De Nolf, W.; Janssens, K. *Analyst* **2014**, *139*, 2489-2498.
(21) Delaney, J. K.; Zeibel, J. G.; Thoury, M.; Littleton, R.; Palmer, M.; Morales, K. M.; de la Rie, E. R.; Hoenigswald, A. *Appl. Spectrosc.* **2010**, *64*, 584-594.
(22) De Nolf, W. *Imaging of crystalline phase distributions by means of scanning and tomographic X-ray powder diffraction*. Ph. D., University of Antwerp, Antwerp, 2013.
(23) De Nolf, W.; Vanmeert, F.; Janssens, K. *J. Appl. Crystallogr.* **2014**, *47*, 1107-1117.
(24) Chiari, G.; Sarrazin, P.; Heginbotham, A. *Appl. Phys. A: Mater. Sci. Process.* **2016**, *122*.
(25) De Nolf, W.; Janssens, K. *Surf. Interface Anal.* **2010**, *42*, 411-418.
(26) Downs, R. T.; Hall-Wallace, M. *Am. Mineral.* **2003**, *88*, 247-250.
(27) Eastaugh, N.; Valentine, W.; Chaplin, T.; Siddall, R. *Pigment Compendium - A dictionary and optical microscopy of historical pigments*; Butterworth-Heinemann, 2008, p 960.
(28) Stols-Witlox, M. In *Studying Old Master Paintings: Technology and Practice*, Spring, M., Ed.; Archetype Publications: London, 2011, pp 284-294.
(29) Aru, M.; Burgio, L.; Rumsey, M. S. *J. Raman Spectrosc.* **2014**, *45*, 1013-1018.
(30) Edwards, H. G. M.; Farwell, D. W.; Perez, F. R.; Villar, S. J. *Appl. Spectrosc.* **1999**, *53*, 1436-1439.
(31) Smieska, L. M.; Mullett, R.; Ferri, L.; Woll, A. R. *Appl. Phys. A* **2017**, *123*, 484.
(32) Lachmann, T.; van der Snickt, G.; Haschke, M.; Mantouvalou, I. *J. Anal. At. Spectrom.* **2016**, *31*, 1989-1997.
(33) Behrens, M.; Girgsdies, F. *Z. Anorg. Allg. Chem.* **2010**, *636*, 919-927.

Authors are required to submit a graphic entry for the Table of Contents (TOC) that, in conjunction with the manuscript title, should give the reader a representative idea of one of the following: A key structure, reaction, equation, concept, or theorem, etc., that is discussed in the manuscript. Consult the journal's Instructions for Authors for TOC graphic specifications.